LIP-STUDENTS-23-31

Study of Flavour Anomalies with the $B^0 \to K^{*0}\mu^+\mu^-$ decay

Pedro Esperanço[1,a]

[1] *Instituto Superior Técnico, Lisboa, Portugal*

Project supervisors: Nuno Leonardo, Alessio Boletti, Matteo Pisano *July 2023*

Abstract. This work aims to study the B^0 meson focusing on the $B^0 \to K^{*0}\mu^+\mu^-$ decay and the calculation of its differential branching fraction. The project is motivated by the fact that several Flavour Changing Neutral Current transitions, such as the decay in study, have shown observables with deviations from Standard Model predictions and which could be the basis to the discovery of new physics. In order to find the differential branching fraction values, this analysis first prepares a model to describe B^0 decay data gathered from proton-proton collision at the LHC with the CMS detector, and then proceeds with the calculation of important observables such as the yield and the detection efficiency of the signal, the $B^0 \to K^{*0}\mu^+\mu^-$ decay. After measuring the differential branching fraction values the results are compared with the Standard Model prediction and previous results.

Keywords: LHC, LFU, differential branching fraction

1 Introduction

The Standard Model (SM) is the most widely accepted physical theory when it comes to the description of the weak, strong, and electromagnetic interactions. Encompassing all known particles and being at the core of several high precision predictions, regarding properties of the $W^\pm$ and Z bosons or the existence of particles such as the third generation quarks and the Higgs boson, it has laid the groundwork for most physical models and experiments. However, albeit successful, the SM is far from complete, not explaining, for example, the existence of gravity, dark matter, or dark energy.

Knowing the SM is not perfect, several experimental studies are constantly being made, not only to try to find clues about what is missing but also to find possible inconsistencies between the theory and reality. One of the vital instruments used in this search for what is known as New Physics (NP) are particle accelerators like the Large Hadron Collider (LHC), the largest particle accelerator in the world situated in a circular tunnel with a circumference of 27km, 100 meters underground across the border between France and Switzerland. Allowing the collision of protons which have been accelerated to reach high values of energy, particle accelerators make possible the observation and study of known particles and the discovery of new ones, possibly beyond the SM.

Given how important these instruments are, it comes as no surprise that huge investments have been made to upgrade them, allowing higher collision energy and higher luminosity, a quantity which measures the number of proton collisions, so as to improve precision. During its first run (2009 to 2013), the LHC was able to achieve 8 TeV of collision energy, then it stopped operation to be upgraded. It started again in 2015 and only finished its second run in 2018, having achieved collision energy of 13 TeV, a value which was further increased to 13.6 TeV during the Run 3 (2022-2025). The High-Luminosity Large Hadron Collider (HL-LHC) is scheduled to start operations in 2029.

NP searches are divided into two categories: direct searches, where NP particles are detected as excesses in distributions, and indirect searches, where NP particles are detected by their effect in other particles such as cross-sections, decay rates and branching fractions. Direct searches are characterized by an increase in the center of mass energy of the collision reaching what is known as high energy frontier while indirect searches are characterized by an increase in luminosity reaching the high precision frontier, which allows the discovery of NP even if they lie at an energy scale well above the collision energy that limit the reach for the direct searches [1].

Through indirect searches, a class of discrepancies with the sector of the SM that deals with particle flavour has been appearing. These are called flavor anomalies and have been detected in two sets of quark level transitions: the Flavor Changing Neutral Current (FCNC) transitions, $b \to sl^+l^-$ (bottom quark to strange quark and oppositely charged leptons), and the Flavor Changing Charged Current (FCCC), $b \to cl\bar{\nu}$ (bottom quark to charm quark, a lepton and neutrino) [1].

Several B meson decay channels are forms of FCNC transitions which have shown observables with deviations from the SM predictions. The LHCb experiment has found the value of the branching fraction ratio $R_{K^+} = \frac{\mathcal{B}(B^+\to K^+\mu^+\mu^-)}{\mathcal{B}(B^+\to K^+e^+e^-)}$ to be 3.1σ away from the predicted value [2]. As shown by the dashed vertical line on Figure 1 the theoretical value of R_{K^+} is 1, meaning the probability of the B meson decaying semi-leptonically into a pair of muons or a pair of electrons should be the same. This could imply the violation of the Lepton Flavor Universality (LFU) which states that the gauge bosons $W^\pm$ and Z have equal couplings to all three lepton flavors [3]. For a deviation from a predicted value to be considered NP it needs to differ from the prediction by at least 5σ. In addition to the study of R_{K^+} and LFU observables from FCNC transitions, discrepancies have been detected in other variables and

[a] e-mail: pedro.esperanco@tecnico.ulisboa.pt

while their significance individually is not large, their correlated interpretation yields higher values of significance, increasing the possibility of finding NP in this sector.

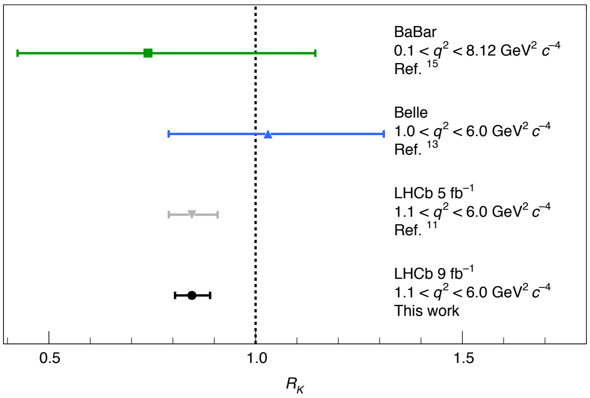

Figure 1: Comparison between the R_{K^+} values measured by the LHCb and the theoretical prediction (vertical dashed line), in addition to the values obtain by the BaBar and Belle collaborations [2].

The focus of this report will be the study of the $B^0 \rightarrow K^{*0}\mu^+\mu^-$ decay and measuring the differential branching fraction of the same decay for different ranges of di-muon invariant mass squared, q^2, which can be used to calculate the ratio $R_{K^{*0}} = \frac{\mathcal{B}(B^0 \rightarrow K^{*0}\mu^+\mu^-)}{\mathcal{B}(B^0 \rightarrow K^{*0}e^+e^-)}$ and compare it to the SM prediction.

2 Analysis framework

2.1 Involved particles

B mesons are hadrons composed of a bottom antiquark, $\bar{b}$, and either an up quark, u, making a B^+, a down quark, d, making a B^0, a strange quark, s, making a B_s^0 or a charm quark, c, making a B_c^+. All of them have their antimeson counterpart where the quarks are switched with the corresponding antiquarks, meaning that the charge value will change sign.

The K^{*0} is an excited state of the K^0 which is composed of a down and anti-strange ($d\bar{s}$) pair of quarks. Before reaching the detector, the K^{*0} decays into a positive kaon, K^+, composed of an up and anti-strange quark pair ($u\bar{s}$) , and a negative pion, π^-, composed of an anti-up and down quark pair ($\bar{u}d$). The decay in study could be more accurately written as $B^0 \rightarrow K^{*0}(K^+\pi^-)\mu^+\mu^-$ evidencing the final products of the decay which actually reach the detector, two oppositely charged leptons ($\mu^+\mu^-$) and two oppositely charged mesons ($K^+\pi^-$).

If the starting B meson is in reality a $\bar{B}^0$ the decay will change to $\bar{B}^0 \rightarrow \bar{K}^*(K^-\pi^+)\mu^+\mu^-$. The fact that the kaon may not always have a positive charge and the pion may not always have negative charge, means that these particles can not be identified by the direction of the curvature of their trajectories alone (explained in 3.1). This can create complications when assigning which particle is the kaon and which is the pion, and since they have different masses, an incorrect tagging will generate a wrong value for the B^0 mass.

Bin number	q^2 range (GeV^2)
0	1-2
1	2-4.3
2	4.3-6
3	6-8.68
4	8.68-10.09
5	10.09-12.86
6	12.86-14.18
7	14.18-16
8	1-6

Table 1: Division into q^2 ranges.

There are two other possible decay channels that have the same final state as this signal. These are the J/ψ decay channel, $B^0 \rightarrow K^{*0}(K^+\pi^-)J/\psi(\mu^+\mu^-)$, which occurs in a lower q^2 region and the $\psi(2S)$ decay channel, $B^0 \rightarrow K^{*0}(K^+\pi^-)\psi(2S)(\mu^+\mu^-)$ which occurs in a higher q^2 region. Despite both particles being composed of a charm and anti-charm quark pair ($c\bar{c}$), they are not the same particle. The $\psi(2S)$ is an excited state of the J/ψ. These two decay channels have very large branching fractions, compared to the signal, meaning they are more likely to occur and are called resonant channels. Despite not being part of our signal they are still used in the analysis since they have already been thoroughly studied. The J/ψ channel will be used as a normalization channel and the $\psi(2S)$ one will be used as a reference and to validate the rest of the analysis.

2.2 Differential branching fraction

As said before, this report aims to find the differential branching fraction of the $B^0 \rightarrow K^{*0}\mu^+\mu^-$ decay for different q^2 ranges. In order to do this there are three steps that should be taken first: dividing the dataset into different q^2 ranges, finding the yield of the decay in the dataset for the different regions, and, using the yield, finding the differential branching fraction.

The q^2 ranges chosen are the same as the ones found in other CMS analysis, allowing the comparison between the results. The reasoning behind the division in this specific ranges can be found elsewhere [1]. The dataset has been divided into bins as shown in Table 1.

Bins 4 and 6 correspond to the J/ψ and $\psi(2S)$ regions respectively. Bin 8 is of particular importance as it represents the region in which theoretical predictions are more robust.

The yield of the signal by q^2 range represents the number of events from the $B^0 \rightarrow K^{*0}\mu^+\mu^-$ decay in the respective bin. It can be calculated through the following expression

$$Y = N_T \mathcal{B} \mathcal{E} \tag{1}$$

where N_T is the total number of produced B^0 mesons, $\mathcal{B}$ is the branching fraction of the decay, $\mathcal{B}(B^0 \rightarrow K^{*0}\mu^+\mu^-)$, by q^2 range, which measures the probability of that specific decay happening in the corresponding bin, and $\mathcal{E}$ represents the efficiency. Since Y, $\mathcal{B}$ and $\mathcal{E}$ all depend on q^2 range, an index is used when referring to these variables. Y_i, $\mathcal{E}_i$ and $\mathcal{B}_i$ represent, the yield, efficiency and branching fraction, $\mathcal{B}(B^0 \to K^{*0}\mu^+\mu^-)$, for the bin number i. For bins 4 and 6, the indexes J/ψ and $\psi(2S)$ are, respectively, used instead for easier understanding of the region being referred to.

During the analysis the yield and efficiency values will be obtained from real and simulated data. However in order to find the branching fraction value the total number of B^0 mesons is still needed, and while it is possible to estimate it knowing the luminosity produced (amount of proton-proton collisions) and the B^0 cross-section (probability of the collisions producing a B^0), it would not be a very precise value. This is where the normalisation channel comes into play. Since this J/ψ channel has been thoroughly studied its branching fraction value can be taken from the Particle Data Group (PDG) and used as a constant to calculate N_T which, being independent of q^2 range, can be used to calculate the other branching fraction values. N_T can be written as

$$N_T = \frac{Y_{J/\psi}}{\mathcal{B}_{J/\psi}\mathcal{E}_{J/\psi}} \tag{2}$$

Manipulating equation 1 to give the branching fraction

$$\mathcal{B}_i = \frac{Y_i}{\mathcal{E}_i N_T} \tag{3}$$

and applying equation 2, the branching fraction of the bin i becomes

$$\mathcal{B}_i = \frac{Y_i}{\mathcal{E}_i}\frac{\mathcal{E}_{J/\psi}}{Y_{J/\psi}}\mathcal{B}_{J/\psi} \tag{4}$$

Dividing the branching fraction value by the size of the q^2 bin the differential branching fraction value by q^2 range, $\left.\frac{d\mathcal{B}}{dq^2}\right|_i$ is obtained

$$\left.\frac{d\mathcal{B}}{dq^2}\right|_i = \frac{Y_i}{\mathcal{E}_i}\frac{\mathcal{E}_{J/\psi}}{Y_{J/\psi}}\frac{\mathcal{B}_{J/\psi}}{\Delta q_i^2} \tag{5}$$

where Δq_i^2 represents the difference between the maximum and minimum q^2 value of bin i.

3 Data acquisition and selection

This analysis uses proton-proton collision data with an energy of $\sqrt{s}$ = 13 TeV collected by the CMS experiment at the LHC in 2018.

3.1 The detector

The Compact Muon Solenoid (CMS) experiment is one of four large experiments at the LHC at CERN. It has a wide range of physics goals and uses data collected through a cylindrical detector positioned surrounding the center of one of the collision points of the LHC.

The detector is composed of 5 main components as shown in Figure 2: the solenoid magnet, the silicon tracker, the Electromagnetic Calorimeter (ECAL), the Hadron Calorimeter (HCAL) and the muon chambers.

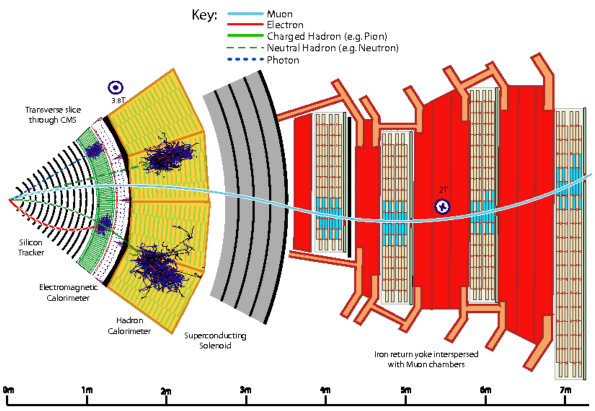

Figure 2: Representation of the different components of the CMS detector. Source [4].

The solenoid magnet is formed by a cylindrical coil of superconducting fibres which can generate a magnetic field of around 4 T. This magnetic field allows the distinction between the charges of particles, as oppositely charged particles will turn to opposite sides; moreover, it makes it possible to calculate the momentum of these particles through the radius of the helical path they follow since a charged particle moving perpendicularly to a magnetic field will have momentum, p, proportional to the radius of said circular path [5].

The silicon tracker allows the tracking of charged particles paths. Whenever one such particle touches the tracker it interacts electromagnetically producing a hit. These hits that happen all throughout the tracker's 75 million electronic sensors can be joined together to rebuild the particles' tracks [5].

Both calorimeters are used to measure the energy of the particles that result from the proton-proton collision. Photon and electron energy is measured by the ECAL which simply stops them and saves the energy needed to do so. The HCAL measures the energy of the hadrons [5].

Lastly, the muon chambers are composed of several muon sub-detectors. Since these particles just pass through the calorimeters without leaving much energy behind it was needed to create this region of the detector. Here, the direction of the magnetic field is inverted, meaning the arc made by the muon's trajectory also inverts its direction. Using the information given by the tracker and these chambers, the path travelled by the muons can be recreated and from there its momentum [6].

3.2 Data selection

Since not all of the information acquired through proton-proton collision can be stored or is necessarily useful for the analysis there are several cuts and triggers applied to the amount of information collected. The first trigger is at the hardware level, it is called Level 1 (L1) trigger and only stores information from events where 2 muons of opposite charges were detected while also imposing constraints in said muons transverse momentum, p_t, based on their pseudorapidity, η, a parameter that describes the angle of a particle relative to the beam axis.

Then, there is a trigger at the software level called High Level Trigger (HLT) where the information will only be stored if both oppositely charged muons were again detected, if a charged hadron was also detected and if the origin point of the tracks of these three particles coincides while not being the same as the collision point. Since the B^0 exists for a period of time and then decays into these particles they should not come from the collision point.

Afterwards there are cuts applied to the data in order to remove most background. Is consists mainly on combinatorial background, meaning that all of the final products of the signal decay were detected, hence why it was considered an event, but at least one of them did not come from a B^0 decay. The background removal itself is done through Multi Variable Analysis (MVA) with Boosted Decision Trees (BDT).

Lastly there is the need to remove contamination from the resonant decay channels of the J/ψ and the $\psi(2S)$ (bins 4 and 6 respectively). One of the reasons behind this contamination is final state radiation (FSR), when a muon emits a photon creating a loss in total energy collected, which can be translated by the detector as a lower q^2 value. In this case events that corresponded to bins 4 and 6 will be assigned to bins 3 and 5. The opposite is also possible, scattering events could cause a muon's trajectory to change making it seem like it had a higher momentum value than it really had and causing the detector to read that as a higher q^2 value contaminating the bins 5 and 7. However, if any of these phenomena happen, the mass reconstruction of the B^0 meson will not give the expected value. In order to remove the contaminating events a cut is made to the non-resonant bins where if the B^0 mass calculated in an event is not the mean value and if the difference to the mean, when applied to the di-muon invariant mass, would bring the event to the q^2 range of one of the resonant channels, that event would be discarded. There is no need to worry about non-resonant decay channels contaminating each other since those have very little events and the probability of it happening is very low.

3.3 Monte Carlo simulation

In order to better study this process Monte Carlo simulations have been made where several B^0 mesons were generated and a large number of events from decay channel $B^0 \rightarrow K^{*0}\mu^+\mu^-$ could be observed, for the different q^2 ranges. This alone would not be a good representation of our experiment, since in reality there is no way to know with complete certainty the trajectory of every particle or even which particles are which, and in the simulation we do. To reduce the gap between the simulation data and the real data, these perfectly defined events are then analyzed as if they had gone through the CMS detector and all the same cuts and triggers are applied. This way the final product of the simulation will be much similar to the real data and the information about the actual results of the simulation are still stored.

The simulated data can then be used to prepare the model with which the real data will be studied. The simulations employed in this analysis were generated with Pythia.

4 The model

4.1 Probability density function

The most important observable for determining the signal yield is the invariant mass of the final state particles. The signal candidates will have a resonant shape while the background will be structureless and by fitting this quantity it is easy to estimate the amount of signal and background events. The distribution of the events along the B^0 candidate's mass can be described with a probability density function (PDF), $\mathcal{P}(m; \vec{p})$ where m is the mass value, $\vec{p}$ are the parameters used and $\mathcal{P}$ gives the probability of a B^0 that decayed through the channel $B^0 \rightarrow K^{*0}\mu^+\mu^-$ having mass m. This value can be re-normalized to adjust to the registered number of events. The PDF can be adjusted to the data and the values of the parameters are then found.

4.2 Likelihood function

In order to find the parameter values, the maximum likelihood theorem is used. It states that the p_i values that maximize the likelihood function, $\mathcal{L}(\vec{p})$, are the ones that give the best fit, meaning they are the ones which maximize the likelihood of the model corresponding to the data. Having N_e total events the likelihood function can be defined as

$$\mathcal{L}(\vec{p}) = \prod_{i}^{N_e} \mathcal{P}(m_i, \vec{p})\,. \tag{6}$$

Although in simple cases it can be done analytically, the maximisation of the likelihood function is performed numerically and, in an attempt to simplify the computation process, the negative of the logarithm, $-ln(\mathcal{L})$, is used and minimized, since products become sums of logarithms which are generally easier to compute [1].

In order to find the error associated with the value chosen for a parameter, p_i^c, the Taylor series expansion around the point p_i^c can be used. Since this point is a minimum of the expression, the first derivative term will be equal to zero and by ignoring terms of order superior to 2, we get

$$-ln(\mathcal{L}(p_i)) = -ln(\mathcal{L}(p_i^c)) - \frac{1}{2}\frac{d^2 ln(\mathcal{L})}{d^2 p_i}\bigg|_{p_i=p_i^c}(p_i - p_i^c)^2\,, \tag{7}$$

which is equivalent to

$$\mathcal{L}(p_i) = c \times e^{\frac{1}{2}\frac{d^2 ln(\mathcal{L})}{d^2 p_i}\big|_{p_i=p_i^c}(p_i-p_i^c)^2}\,, \tag{8}$$

and shows that the likelihood function follows a Gaussian distribution with σ^2 equal to $\left(-\frac{d^2 ln(\mathcal{L})}{d^2 p_i}\right)^{-1}\bigg|_{p_i=p_i^c}$, meaning that the error associated with p_i^c is given by $\left(-\frac{d^2 ln(\mathcal{L})}{d^2 p_i}\right)^{-\frac{1}{2}}\bigg|_{p_i=p_i^c}$.

When extracting more than one parameter from a fit, the error is calculated with the covariance matrix K_{ij}, whose entries measure how much two parameters, p_i, p_j vary together and are given by

$$K_{ij} = \left(-\frac{d^2 ln(\mathcal{L})}{dp_i dp_j}\right)^{-1}\Bigg|_{\vec{p}=\vec{p}^c} . \tag{9}$$

The statistical error of a chosen parameter, p_i^c can be found by looking at the diagonal of K and taking the square root of the value, $\sigma_i = \sqrt{K_{ii}}$ [1].

4.3 Modelling the signal peak

Two models were prepared for this analysis: the Gaussian model (GM) and the CB model (CBM).

4.3.1 Gaussian Model

In this model, the PDF is computed as a sum of two Gaussian PDFs, given by (modulo normalizations)

$$\mathcal{P}_{Gauss}(m; \bar{m}, \sigma_1, \sigma_2, \gamma) = \gamma e^{-\frac{1}{2}\left(\frac{m-\bar{m}}{\sigma_1}\right)^2} + (1-\gamma)e^{-\frac{1}{2}\left(\frac{m-\bar{m}}{\sigma_2}\right)^2}, \tag{10}$$

where m represents the variable, in this case the mass, $\bar{m}$ represents the mean mass value, σ_1 and σ_2 represent the standard deviation and γ is a fraction between the two components that guarantees the normalization of the final PDF and belongs to the interval (0, 1).

4.3.2 CB Model

In this model, the PDF is computed as sum of a Gaussian PDF and a Crystal Ball function which is defined as $CB(m; \bar{m}, \sigma, n, \alpha) =$

$$= \begin{cases} e^{-\frac{t^2}{2}}, & \text{if } t > -\alpha \\ \left(\frac{n}{|\alpha|}\right)^n e^{-\frac{\alpha^2}{2}} \left(\frac{n}{\text{mod } |\alpha|} - |\alpha| - t\right)^{-n}, & \text{if } t \leq -\alpha \end{cases} \tag{11}$$

with $t = \frac{m-\bar{m}}{\sigma}$.

The final expression for the CBM PDF becomes

$$\mathcal{P}_{CB}(m; \bar{m}, \sigma_1, \sigma_2, \alpha, n, \gamma) = \gamma e^{-\frac{1}{2}\left(\frac{m-\bar{m}}{\sigma_1}\right)^2} + (1-\gamma)CB(m; \bar{m}, \sigma_2, n, \alpha) \,. <<<<< - \tag{12}$$

4.3.3 Model Comparison

The GM assumes the B^0 mass follows a normal distribution, which, considering the central limit theorem would not be a bad approximation. However it is clear to see in Figure 3 (up) that the fit fails to describe some points on the left side of the mean value. It is a sum of two PDFs representing the fact that different regions of the detector have different precision and that B^0 meson decay products with different momentum or that followed different trajectories may be harder to track. One of the Gaussians represents more precisely measured mass values (smaller σ) and the other represents less precisely measured mass values (greater σ).

The CBM also takes into account more or less precisely measured masses, but the crystal ball component makes it so that the left part of the Gaussian decreases in a slower manner, which makes for a better fit (see Figure 3 down) and can be explained by the physical process known as the Bremsstrahlung effect, where charged particles moving at high speed through matter emit photons, thus loosing some energy which will not be taken into account during the process of B^0 mass reconstruction.

The CBM was the one chosen as the nominal for the analysis.

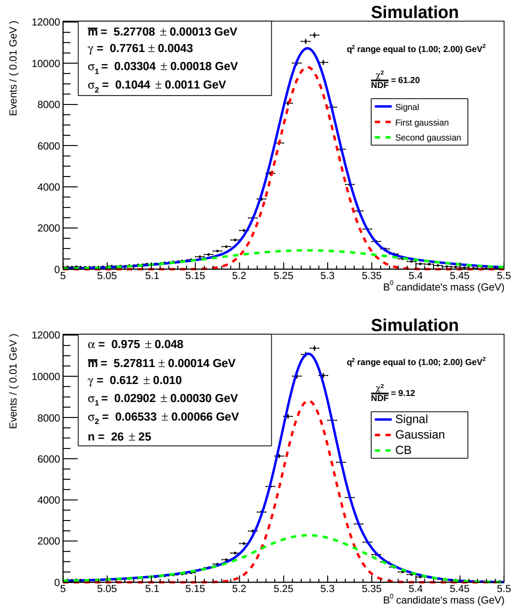

Figure 3: Fit to Monte Carlo data in bin 0 with Gaussian Model (up) and CB Model (down).

5 Finding the yield

The main difference between simulated data and real data is the big amount of background that, despite all the cuts and triggers applied, will always be present in real data. This means that the model as is can not yet be used to describe the data. The background is assumed to follow an exponential curve and is added as

$$\mathcal{P}_b(m; \lambda) = \mathcal{N} e^{\lambda m} \tag{13}$$

where $\mathcal{N}$ is a normalization constant that depends on the range to normalize the PDF.

The global PDF, $\mathcal{P}_G$, is then defined as

$$\mathcal{P}_G = Y_s \mathcal{P}_{CB} + Y_b \mathcal{P}_b \tag{14}$$

where Y_s and Y_b represent the yields of the signal and the background respectively. It is important to notice that this time two parameters are being used to normalize the sum of the PDFs. It happens because $\mathcal{P}_G$ will be used for an extended fit, meaning the likelihood function will have an additional factor, becoming

$$\mathcal{L}(\vec{p}) = \prod_i^{N_e} \mathcal{P}(m_i, \vec{p}) \times \frac{e^{-(Y_s+Y_b)}(Y_s + Y_b)^{N_e}}{N_e!} \tag{15}$$

This additional factor constrains the signal and background yields to follow a Poisson distribution.

By fitting this model to the data the yield of the signal, Y_s, can be extracted as shown in Figure 4.

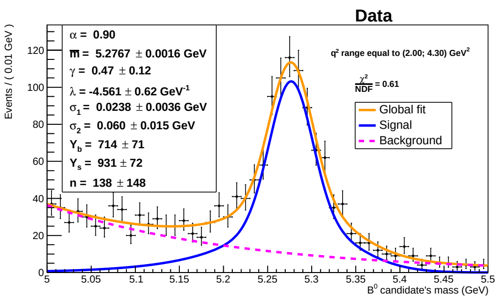

Figure 4: Fit to data with the CBM in bin 1.

In Figure 5 it is possible to observe the yield of the signal in the different bins.

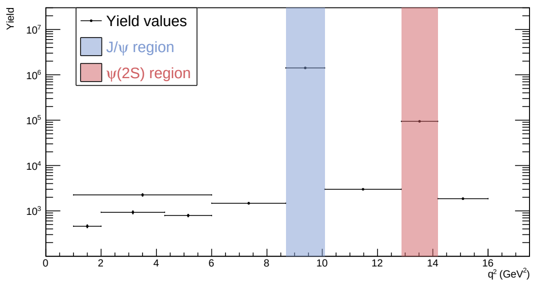

Figure 5: Yield values for the different q^2 ranges.

6 Efficiency

The efficiency, $\mathcal{E}$, is computed as the number of signal events in a specific q^2 range after all the cuts and triggers over the total number of signal events in that same q^2 range. Even though the numerator of this fraction could be obtained in the real data there would be no way to find the denominator. However, both values can be obtained with the information stored after the Monte Carlo simulations. Since during the simulation process every variable is perfectly known, the total number of B^0 mesons that decayed according to the signal can be stored, and considering the simulation results are made to go through the CMS detector and all the cuts and triggers, the number of events detected is very similar to what it would be were it real data with the same number of total events. The efficiency values by q^2 range can be seen in Figure 6.

Looking at Figure 6 it becomes evident that efficiency values increase for higher q^2 values; indeed, di-muons with an higher invariant mass tend to produce muons with higher transverse momentum, p_t, and particles with higher p_t are generally easier to detect. It is also possible to notice that efficiency values from bins 3, 5 and 7 seem

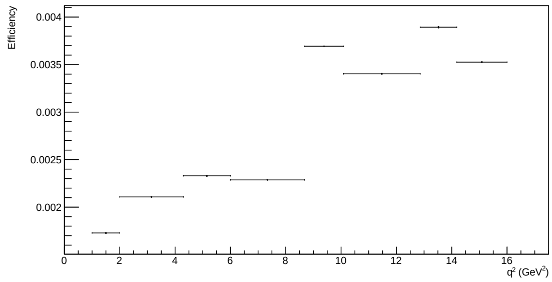

Figure 6: Efficiency values for different q^2 regions

to have been shifted down or have lower values than expected, considering the values for other bins. This can be explained by the cut made to reduce the contamination from the resonant decay channels (bins 4 and 6) Despite not being the only bins where the cut was applied these three bins were the only ones affected by the cut due to being adjacent to the J/ψ and $\psi(2S)$ regions and the effect of the cut being limited in q^2.

7 Systematic uncertainties

There are three different sources to the systematic uncertainties in the values presented in Section 8.

The first source is the branching fraction of the normalisation channel. Due to the existence of uncertainties associated with the branching fraction values taken from the PDG averages, these uncertainty values had to be propagated to the total error of this analysis results. The second source of uncertainties are the efficiencies. The propagation of the statistical fluctuation of the simulated sample is done and applied to the result. Lastly there is the bias being introduced to the result when making the choice of which model to use to fit the data. Despite not being used in the analysis the Gaussian model still does a fairly good description of the real data, and for this reason, as a way to estimate the bias introduced, the difference between the yield value given by the two models is also used to check how much of a difference in the result it would make. Figure 7 shows a fit with the Gaussian Model (up) and one with the CB Model (down) to bin 1 where it is possible to see that both models describe the data well.

8 Results

Using the calculated yield and efficiency values it is possible to obtain the values of the branching fraction by q^2 range using Equation 4. In Figure 8, it is visible that the obtained value for the branching fraction for the $\psi(2S)$ region is well within the uncertainty of the value from the PDG which attests the robustness of the analysis procedure.

By dividing the branching fraction values by their respective bin size the differential branching fraction values are reached. These analysis results have been plotted in Figure 9 in addition to the values obtained with a CMS

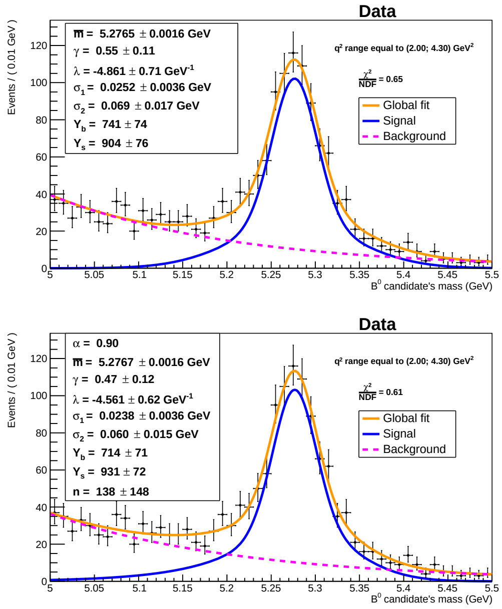

Figure 7: Fit to data in bin 1 with Gaussian Model (up) and CB Model (down).

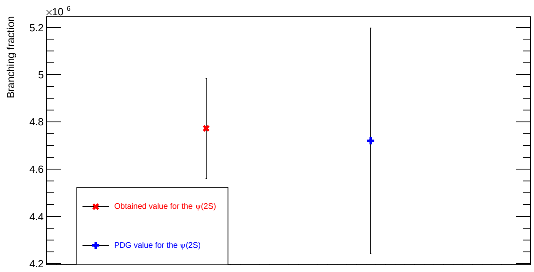

Figure 8: Comparison between this analysis result and the PDG value of the Branching Fraction for the ψ(2S) region

dataset collected in 2012 (during Run 1 at the LHC) [7], an outdated SM prediction also done with the CMS binning [8, 9] and a more recent SM prediction only available with the q^2 binning done by the LHCb experiment [10]. It is important to note that the Run 1 result binning is the same as this analysis binning, and the only reason why the point is shifted to the side and not at the center of the bin is so it would be possible to compare the error bars between that result and this analysis result.

The differential branching fraction values by q^2 range can be found in Table 2. The result for bin 8 is not shown in Figure 9 as it would crowd the image due to its larger bin size, but is present in the aforementioned table. As mentioned in Section 2.2, theoretical predictions are more robust in bin 8, the SM prediction in this q^2 range is equal to $3.2^{+1.2}_{-1.0} \times 10^{-8}$ GeV^{-2} ([8, 9]), which when compared with this analysis result shows that it is well within the predicted value uncertainty range.

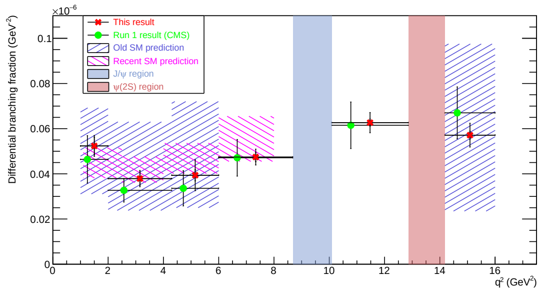

Figure 9: Comparison between this analysis branching fraction values and the values from a Run 1 experiment (source [7]), an outdated SM prediction (source [8, 9]) and a more recent SM prediction (source [10]).

9 Conclusion

This analysis focused on the study of the $B^0 \to K^{*0}\mu^+\mu^-$ decay due to the propitiousness shown by FCNC transitions to reveal physics beyond the SM and possible LFU violations. The main goal of the analysis lies in finding the differential branching fraction values of the decay in different q^2 ranges. These values could be further used to calculate the branching fraction ratio $R_{K^{*0}} = \frac{\mathcal{B}(B^0\to K^{*0}\mu^+\mu^-)}{\mathcal{B}(B^0\to K^{*0}e^+e^-)}$ in order to check whether there is or not a big deviation from the SM prediction and whether or not LFU is violated.

This analysis was able to produce differential branching fraction values by q^2 range with increased precision than the ones of the 2012 CMS experiment [7] (Figure 9), which can be explained by the upgrades done to the LHC and CMS between Run 1 and Run 2. The fact that the branching fraction value in the $\psi(2S)$ region (bin 6) is very similar, less than 1σ away, to the value on the PDG (Figure 8) gives increased confidence in the results obtained.

These results do not reveal significant discrepancies with the SM predictions, although it is also true that these predictions come with sizable uncertainties

The work may be extended by repeating the analysis using the electron channel decay, $B^0 \to K^{*0}e^+e^-$. Using the differential branching fraction values from both decay channels, the ratio $R_{K^{*0}} = \frac{\mathcal{B}(B^0\to K^{*0}\mu^+\mu^-)}{\mathcal{B}(B^0\to K^{*0}e^+e^-)}$ by q^2 can be calculated and then compared to the SM prediction which is much more precise for this observable. Furthermore, such a robust observable allows to directly test the LFU principle.

10 Acknowledgments

I would like to thank the three supervisors who guided me throughout this project, Nuno Leonardo, professor at IST and researcher at LIP, Matteo Pisano, professor at IST and researcher at LIP and finally the one who, despite not being associated with IST, served as main supervisor, Alessio Boletti, researcher at LIP, for allowing me to partake in this project and for the many insights the three of them gave me not only about this analysis but about High Energy Physics in general.

Bin number	DBF $\times 10^{-8}$ (GeV^{-2})	σ_{stat} $\times 10^{-8}$ (GeV^{-2})	σ_{syst} $\times 10^{-8}$ (GeV^{-2})	σ_{PDG} $\times 10^{-8}$ (GeV^{-2})
0	5.24	0.38	0.15	0.21
1	3.79	0.29	0.14	0.15
2	3.94	0.25	0.62	0.16
3	4.74	0.20	0.22	0.19
5	6.27	0.16	0.33	0.25
7	5.71	0.18	0.44	0.23
8	4.24	0.27	0.19	0.17

Table 2: Differential branching fraction values by bin number and their statistic and systematic uncertainties, and at the rightmost column the systematic uncertainty associated with the usage of the branching fraction value of the J/ψ from the PDG.

References

[1] M.C. Feliciano Faria, *Investigating the flavour anomalies through the rare beauty decay $B^0 \to K^{*0}\mu^+\mu^-$*, https://cds.cern.ch/record/2791778 (2021), presented 22 Oct 2021

[2] Nature Physics **18**, 277 (2022)

[3] R. Aaij et al. (LHCb), Nature Phys. **18**, 277 (2022), 2103.11769

[4] A.M. Sirunyan et al. (CMS), JINST **12**, P10003 (2017), 1706.04965

[5] *Detector | CMS Experiment — cms.cern*, https://cms.cern/detector, [Accessed 05-Jun-2023]

[6] *Detecting Muons | CMS Experiment — cms.cern*, https://cms.cern/detector/detecting-muons, [Accessed 05-Jun-2023]

[7] V. Khachatryan et al. (CMS), Phys. Lett. B **753**, 424 (2016), 1507.08126

[8] C. Bobeth, G. Hiller, D. van Dyk, JHEP **07**, 098 (2010), 1006.5013

[9] C. Bobeth, G. Hiller, D. van Dyk, Phys. Rev. D **87**, 034016 (2013), 1212.2321

[10] N. Gubernari, M. Reboud, D. van Dyk, J. Virto, Journal of High Energy Physics **2022** (2022)

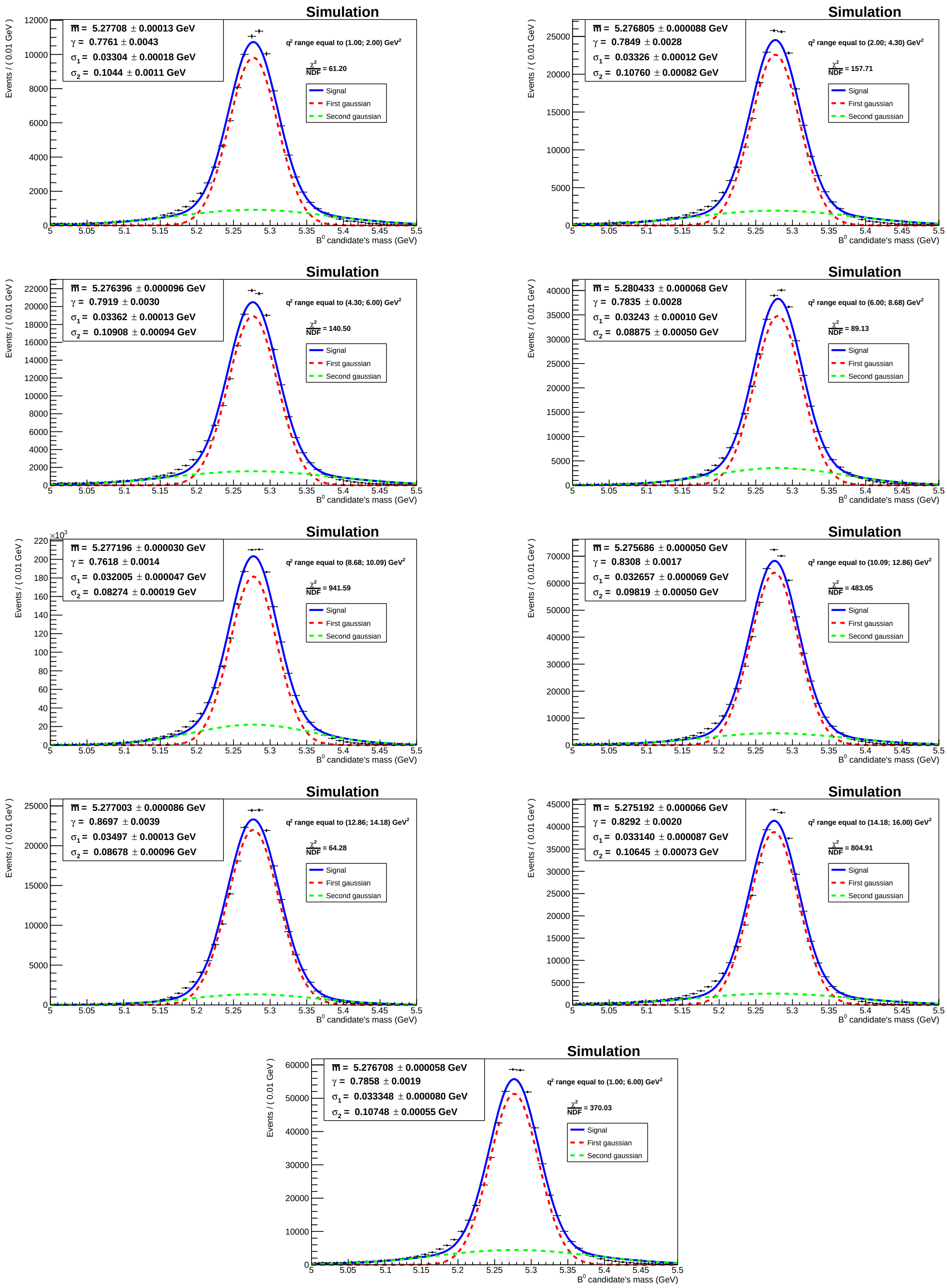

Figure 10: Fit to Monte Carlo simulation with the GM in every bin.

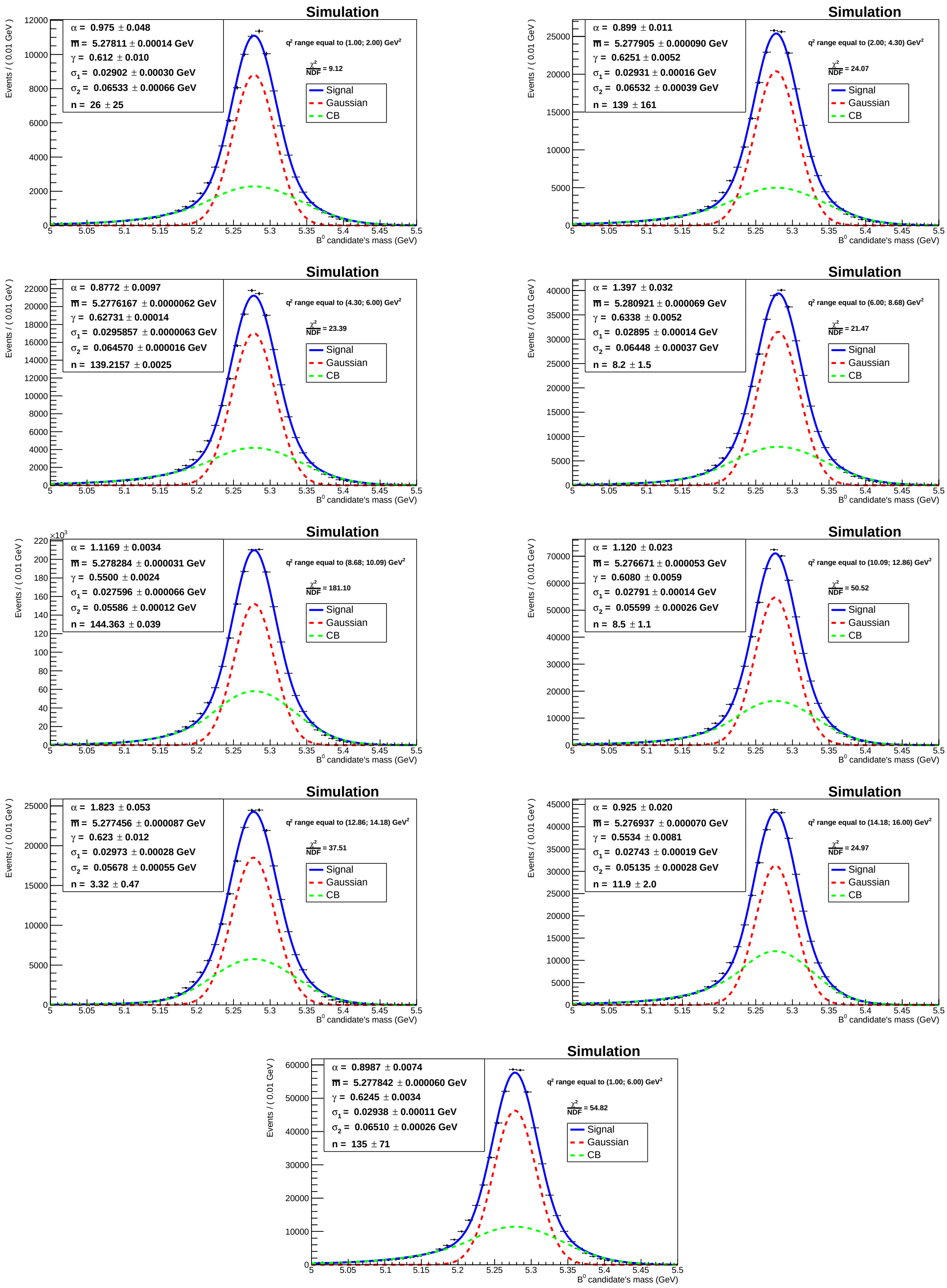

Figure 11: Fit to Monte Carlo simulation with the CBM in every bin.

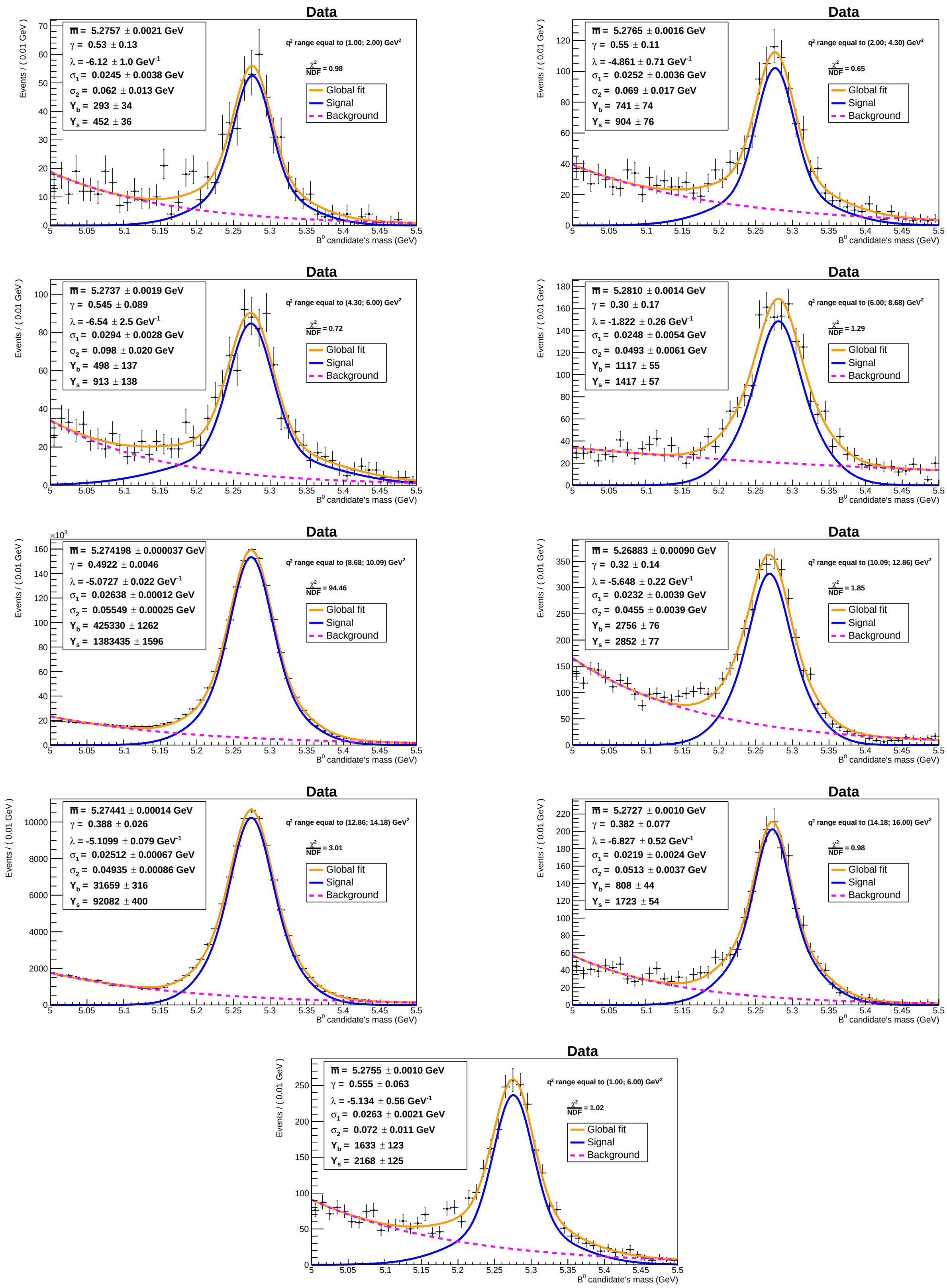

Figure 12: Fit to CMS data with the GM in every bin.

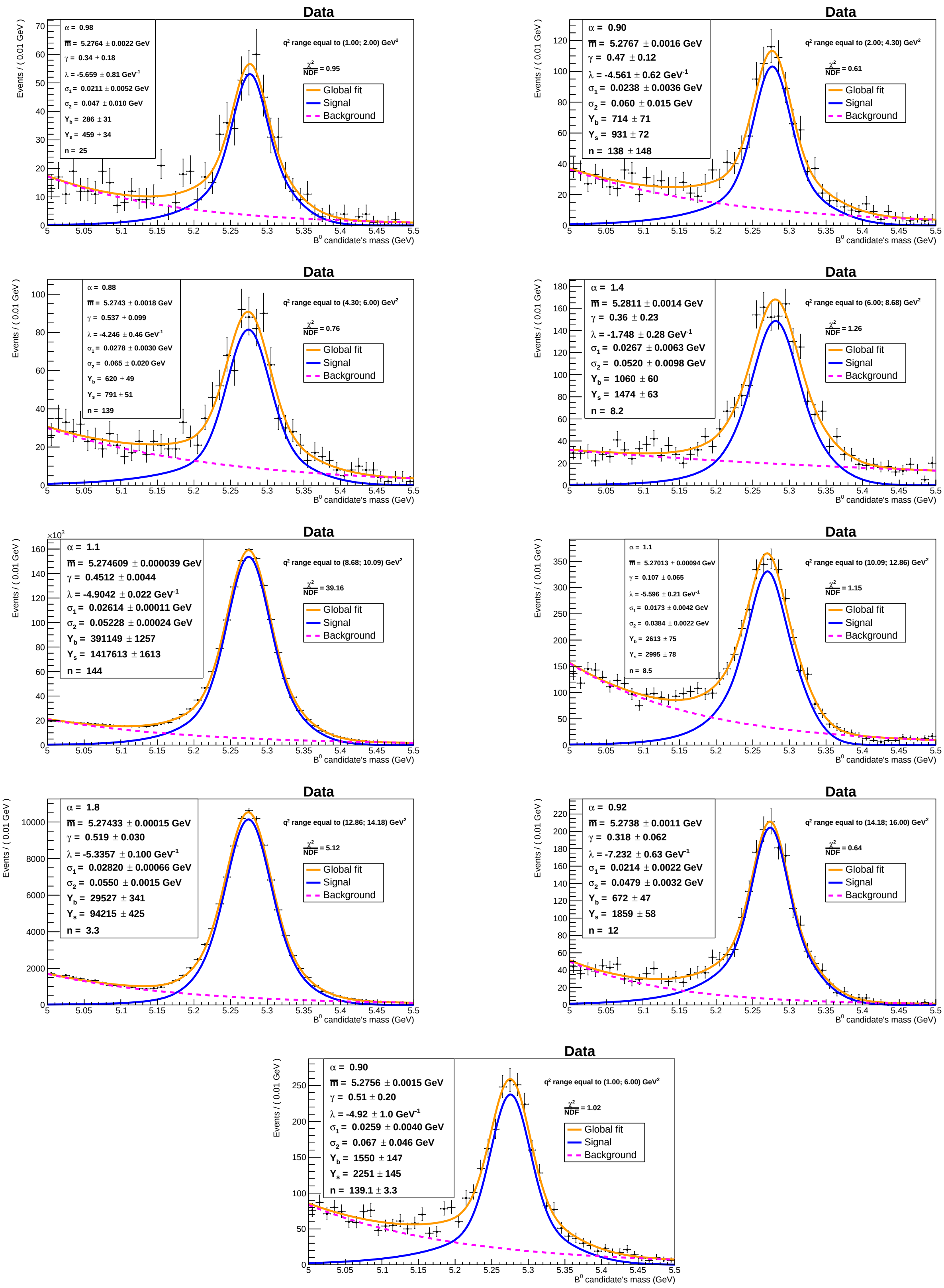

Figure 13: Fit to CMS data with the CBM in every bin.